
Article:
Nawaz, Syed Junaid, Wyne, Shurjeel, Baltzis, Konstantinos et al. (2 more authors) (2017) A Tunable 3-D Statistical Channel Model for Spatio-temporal Characteristics of Wireless Communication Networks. Transactions on Emerging Telecommunications Technologies. pp. 1-20. ISSN 2161-3915

https://doi.org/10.1002/ett.3213

TRANSACTIONS ON EMERGING TELECOMMUNICATIONS TECHNOLOGIES
Trans. Emerging Tel. Tech. 2016; **00**:1–20
DOI: 10.1002/ett

RESEARCH ARTICLE

A Tunable 3-D Statistical Channel Model for Spatio-temporal Characteristics of Wireless Communication Networks

Syed Junaid Nawaz[1]*, Shurjeel Wyne[1], Konstantinos B. Baltzis[2], Sardar M. Gulfam[1], and Kanapathippillai Cumanan [3].

[1]Department of Electrical Engineering, COMSATS Institute of Information Technology (CIIT), Islamabad, Pakistan.
[2]Department of Physics, Aristotle University of Thessaloniki, Greece.
[3]Department of Electronics Engineering, University of York, United Kingdom.
junaidnawaz@ieee.org, *shurjeel.wyne@comsats.edu.pk*, *kbaltzis@auth.gr*, *sardar_muhammad@comsats.edu.pk*, and *kanapathippillai.cumanan@york.ac.uk*

ABSTRACT

A new three-dimensional (3-D) geometric channel model is proposed with multiple degrees of freedom in its scattering volume geometry, which enables accurate modeling of realistic propagation scenarios for emerging Machine-to-Machine (M2M) wireless networks. Analytical expressions for the joint and marginal statistics in delay and angular domains are derived and we present the impact of various physical channel parameters such as link distance, antenna heights, size and position of scattering region, as well as shape and orientation of scattering region on delay and angular spread of the proposed model. The derived analytical results are validated with simulations and are also shown to provide a good fit to published empirical data-sets. Relative to existing models, the proposed model is shown to more accurately adapt to different propagation environments envisioned for emerging communication scenarios such as in indoor pico-cellular and Vehicle-to-Vehicle (V2V) communication applications. Copyright © 2016 John Wiley & Sons, Ltd.

***Correspondence**

Email: junaidnawaz@ieee.org, Address: Department of Electrical Engineering, COMSATS Institute of Information Technology (CIIT), Islamabad, Pakistan.

1. INTRODUCTION

Significant research interest has been recently devoted to emerging paradigms of wireless networks encountered in Machine-to-Machine (M2M) communications; these include application scenarios such as intelligent transport systems, smart metering, and remote health diagnostics [1, 2, 3]. A real-world performance evaluation of M2M communications necessitates an appropriate understanding of the relevant propagation scenario in terms of the Angle-of-Arrival (AoA) and Time-of-Arrival (ToA) information of multipath components of the wireless propagation channel. For this purpose geometry-based stochastic channel models have been extensively studied in the literature for conventional cellular systems in which a fixed Base-Station (BS) communicates with a Mobile-Station (MS) [4, 5, 6]. Since geometric channel models inherently establish probabilistic relations between spatial locations of the Transmit (Tx), Receive (Rx), and scatterers to model wireless propagation, it becomes imperative to investigate the distributions of the multipath ToA, AoA, and Angle-of-Departure (AoD) to gain insights into the physics of any novel geometric channel model. For this reason the problem of determining the multipath delay and angular distributions has received significant attention in the literature, see for example [7, 8, 9, 10] and

Prepared using ettauth.cls [Version: 2012/06/19 v2.10]

references therein. Angular and temporal characteristics of a radio propagation channel are necessary for a realistic performance evaluation and designing of a mobile radio communication system. The spread of a channel in temporal and angular domains helps in determining frequency and space selective nature of the channel, respectively. The angular spread quantified in terms of multipath shape factors (i.e., angular Spread, angular constriction and direction of maximum fading) helps in determining second order fading statistics of the channel; the second order fading statistics include, level crossing rate, average fade duration, coherence distance, and spatial correlation [11, 12]. Such characterization of fading statistics assists in devising efficient schemes at Tx and Rx nodes for interleaving, coding, and equalization algorithms.

Unlike conventional cellular systems that have BS antenna heights above or at rooftop levels, the antenna heights of M2M nodes are expected to be typically much lower than the surrounding scatterers such as buildings, trees, and other objects. For example in Vehicle-to-Vehicle (V2V) channels, which constitute a special case of M2M communications, this differing propagation environment has led to many investigations into appropriate two-dimensional (2-D) and three-dimensional (3-D) models [13, 14, 15, 16, 17, 18]. In [13], a uniform distribution of scatterers in circular regions is assumed around each MS and the ToA and AoA statistics are investigated. In [14], a scattering model for V2V scenarios is presented in which the scatterers are confined to elliptical regions and closed-form expressions for the distribution of AoA and ToA are derived. In [15], a more general 2-D elliptical model is proposed for V2V channels by assuming the scatterers to be uniformly distributed within adjustable hollow ellipses around each MS and the distribution of the AoA at each MS is then derived.

Subsequent investigations have revealed that low antenna heights of the communicating nodes result in signal reflections from nearby scatterers that are more elevated than the communicating antennas. This makes it necessary to include the elevation plane for an accurate description of the relevant propagation channels. In V2V channel modeling efforts, various 3-D channel models have been previously proposed for a more precise spatio-temporal description of the propagation scenario, see [16, 17, 18] and references therein. In [16], a 3-D multiple-input-multiple-output model for V2V channels is proposed and the authors derive a closed-form joint space-time correlation function for the considered 3-D scattering environment; the effect of space-time correlation on outage capacity of different antenna array configurations is then studied. In [17], a 3-D semi-ellipsoid model is proposed to effectively model V2V channels for urban street canyons. The scatterers are assumed to be uniformly distributed within semi-ellipsoids around each MS and the authors derive closed-form expressions for the AoA jointly in azimuth and elevation. Furthermore, for various street orientations and different elevations of the scatterers the marginal probability density functions (PDFs) of the azimuth and elevation angles are also presented. In [18], the temporal characteristics of a 3-D semi-ellipsoid geometrical channel model for V2V communications is presented. Assuming a uniform scatterer distribution around the MSs, the authors derive closed-form expressions for the joint PDF of the ToA and AoA in azimuth and elevation planes.

The present work is a generalization of the 3-D geometric channel modeling approach of [17, 18] in that a more flexible placement of communicating nodes, relative to their surrounding scatterers, is proposed to admit M2M communication scenarios. Specifically, the novel contributions of this work are:

1. The maximum propagation delay is incorporated into the model through its associated maximum-delay-ellipsoid. The overlap of this ellipsoid with the scattering ellipsoids at Tx and Rx determine the effective scattering volumes at respective link ends.
2. The scattering ellipsoids at Tx and Rx side are independently rotatable in the horizontal plane, about their respective origins. Moreover, the origin of each of these two ellipsoids can be arbitrarily shifted along the vertical axis of the coordinate system.
3. The antennas at Tx and Rx can have a vertical offset relative to the center of their respective scattering regions.
4. Closed-form expressions are derived for the delay distribution, joint and marginal distributions of the AoA in azimuth and elevation of the multipath components of the modeled channel.

Trans. Emerging Tel. Tech. 2016; **00**:1–20
DOI: 10.1002/ett
Prepared using ettauth.cls

Table I: Proposed Model's Input Parameters

Symbol	Definition
h_m	Elevation of antenna employed at node m.
z_m	Vertical displacement of the origin of scattering volume (ellipsoid) around Node m with reference to the ground level.
d	Horizontal separation between N_1 and N_2.
a_m, b_m, and c_m	Major, intermediate, and minor axes of the bounding ellipsoid at node m.
θ_m	Rotation angle (in horizontal plane) in the orientation of bounding ellipsoid around node m.
τ_o and $\tau_{\max}$	Delay associated with LoS and longest propagation path (Minimum and maximum delay).

The remainder of this paper is organized as follows. Sec. II describes the system model of the proposed 3-D geometrical channel model. Furthermore, closed-form expressions for the distributions of delay and AoA are also derived in this section. In Sec. III, a validation of the theoretical results with simulations and published measurement data is presented with relevant discussions. Finally, Sec. IV concludes this work.

2. SYSTEM MODEL

The proposed model provides a high order of Degrees-of-Freedom (DoF) in it's parameters, which enables adjustability of the model according to the targeted propagation environment to obtain realistic channel characteristics. The geometrical composition of the proposed model is illustrated in Fig. 1. Scattering objects in the vicinity of communicating nodes N_m are modeled as bounded within (triaxial) ellipsoidal shaped regions denoted by E_m, where, the subscript m takes value as, $m = 1$ and $m = 2$ to represent the nodes 1 and 2, respectively. The independently adjustable major, intermediate, and minor dimensions of these ellipsoids are represented by a_m, b_m, and c_m, respectively. Moreover, these scattering ellipsoids (E_m) are modeled as independently rotatable about their origin in x-y plane with angles θ_m, where $-\pi/2 \leq \theta_m \leq \pi/2$. The horizontal position of the origin of these scattering ellipsoids (E_m) is fixed at the horizontal position of communication nodes (N_m); however, their origin in vertical plane is designed as shiftable with parameter z_m. The elevation of antennas is denoted by h_m. Difference between the elevation of antennas employed at N_1 and N_2 can thus be found as, $h_e = h_1 - h_2$. The angles observed at a certain node N_m along the arriving multipath component corresponded from a certain scattering point $\mathrm{s_p}$, are denoted by ϕ_m and β_m in azimuth and elevation planes, respectively. The range of azimuth and elevation AoA parameters is, $-\pi \leq \phi_m < \pi$ and $0 \leq \beta_m \leq \pi/2$, respectively. The input geometric parameters are enlisted in Table I. Distance of a certain scattering point $\mathrm{s_p}$ from a communication node N_m is denoted by d_m. Length of the propagation path corresponded from p^{th} scattering point can thus be found as, $l_p = d_1 + d_2$; subsequently, propagation delay of this path can be obtained as $\tau_p = l_p/c$. The parameter c represents the velocity of propagation of electromagnetic waves. The x-axis of the coordinate system is fixed along the azimuth LoS direction (i.e., azimuth LoS angle is fixed at 0^o). The elevation LoS angle can be obtained from the following equation,

$$\beta_{\mathrm{LoS}} = \arctan\left(\frac{h_e}{d}\right). \tag{1}$$

The horizontal and Line-of-Sight (LoS) distance from N_1 to N_2 is d and d_{LoS}, respectively.

$$d_{\mathrm{LoS}} = \sqrt{d^2 + h_e^2}. \tag{2}$$

One of the unique properties of an (oblate) ellipsoid is that the sum of distances from its (two) foci points to any point on its surface is the same. Exploiting this property, an ellipsoid (ξ_τ) can be drawn corresponding to a certain propagation delay τ with its foci points at N_1 (Tx) and N_2 (Rx). The effective scattering region (ESR) for delay τ is thus the overlapping portion of the scattering ellipsoids (E_m) with the surface of virtual bounding (oblate) ellipsoid (ξ_τ). Similarly, the overall boundary of ESR can be defined by an ellipsoid corresponding to longest propagation delay $\tau_{\max}$. The ESR is thus the union of $\mathrm{R}_{\tau 1}|_{\tau=\tau_{\max}}$ and $\mathrm{R}_{\tau 2}|_{\tau=\tau_{\max}}$, truncated by the ground plane. The major and

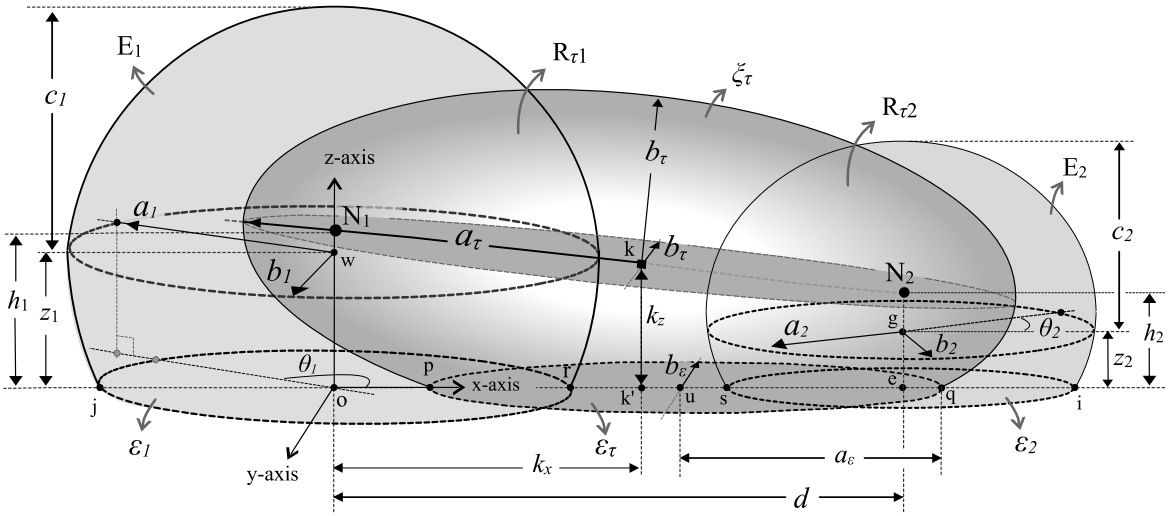

Figure 1: Geometrical composition of proposed 3-D scattering model.

minor dimensions of the bounding (oblate) ellipsoid (ξ_τ) can be calculated from the given delay τ, as given under,

$$a_\tau = \frac{c\tau}{2}, \tag{3}$$

$$b_\tau = \frac{1}{2}\sqrt{c^2\tau^2 - d_{\mathrm{LoS}}^2}. \tag{4}$$

The origin of coordinate system is assumed at the base of communication node N_1. The position of N_1 and N_2 can thus be represented in cartesian coordinates as (0,0,h_1) and (d,0,h_2), respectively. The scattering ellipsoids E_1 can be expressed as,

$$\frac{(x\cos\theta_1 - y\sin\theta_1)^2}{a_1^2} + \frac{(y\cos\theta_1 + x\sin\theta_1)^2}{b_1^2} + \frac{(z-z_1)^2}{c_1^2} = 1. \tag{5}$$

The equation for scattering ellipsoid E_2 is given as below,

$$\frac{((x-d)\cos\theta_2 - y\sin\theta_2)^2}{a_2^2} + \frac{(y\cos\theta_2 + (x-d)\sin\theta_2)^2}{b_2^2} + \frac{(z-z_2)^2}{c_2^2} = 1. \tag{6}$$

The spherical coordinates system based representation can be obtained by using the transformation relationships, $x = \rho\cos\beta_m\cos\phi_m$, $y = \rho\cos\beta_m\sin\phi_m$, and $z = \rho\sin\beta_m$, where, ρ is the radial coordinate. The virtual bounding ellipsoid ξ_τ can be expressed in cartesian and spherical coordinates as under,

$$\frac{((x-k_x)\cos\beta_{\mathrm{LoS}} - (z-k_z)\sin\beta_{\mathrm{LoS}})^2}{a_\tau^2} + \frac{y^2}{b_\tau^2} + \frac{((z-k_z)\cos\beta_{\mathrm{LoS}} + (x-k_x)\sin\beta_{\mathrm{LoS}})^2}{b_\tau^2} = 1, \tag{7}$$

where the parameters k_x and k_z represent the shift from the origin (point k) of the ellipsoid ξ_τ to the origin (point o) of the coordinates system along x-axis and z-axis, respectively. These shifts can be expressed as,

$$k_x = -\frac{d_{\mathrm{LoS}}}{2}\cos\beta_{\mathrm{LoS}}, \tag{8}$$

$$k_z = -h_1 + \frac{d_{\mathrm{LoS}}}{2}\sin\beta_{\mathrm{LoS}}. \tag{9}$$

The ESR is union of regions $\mathrm{R}_{\tau 1}$ and $\mathrm{R}_{\tau 2}$, formed with the overlapping of scattering ellipsoids E_1 and E_2 with the virtual bounding ellipsoid ξ_τ. The volume of region $\mathrm{R}_{\tau 1}$ can be obtained by adopting the approach in [19], i.e., adding the volume of intersection of $\mathrm{R}_{\tau 1}$ with infinite elementary pyramidal frustums obtained from four rays originated from N_2 in the directions (ϕ_2, β_2), ($\phi_2 + \Delta\phi_2$, β_2), (ϕ_2, $\beta_2 + \Delta\beta_2$), and ($\phi_2 + \Delta\phi_2$, $\beta_2 + \Delta\beta_2$); where $\phi_2 \ll \Delta\phi_2$ and $\beta_2 \ll \Delta\beta_2$. The volume of $\mathrm{R}_{\tau 2}$ can be obtained with the sum of volume of infinite elementary pyramids originated from N_2. The volume V of illuminated scattering region, for a given delay τ, can thus be obtained by adding the volume of regions $\mathrm{R}_{\tau 1}$ and

DOI: 10.1002/ett
Prepared using ettauth.cls

$\mathrm{R}_{\tau 2}$, which can be expressed as follows,

$$V_\tau(\tau) = \frac{1}{3} \int_{\phi_{t2}^-}^{\phi_{t1}^+} \int_{\beta_l}^{\beta_{t1}^+} \left\{ \left(\rho_{\beta 1}^+\right)^3 - \left(\min(\rho_{\beta 2}^-, \rho_\tau, \rho_e)\right)^3 \right\} \sin\beta_2 \, d\beta_2 \, d\phi_2 + \frac{1}{3} \int_{-\pi}^{+\pi} \int_{-\frac{\pi}{2}}^{\beta_{t4}} \left(\min(\rho_2, \rho_\tau, \rho_e)\right)^3 \sin\beta_2 \, d\beta_2 \, d\phi_2 \tag{10}$$

where $\beta_l = \min(\beta_{t1}^-, \beta_{t3})$. Similarly, the volume of ESR, $V_{\tau_{\max}}$, for a known longest propagation path's delay, $\tau_{\max}$, can be obtained by substituting $\tau_{\max}$ instead of τ in (10). The total accumulated volume of scattering solids can be computed as,

$$V = \max\left(V_{\tau_{\max}}\right) = \tfrac{4\pi}{3}\left(a_1 b_1 c_1 + a_2 b_2 c_2\right) - \frac{\pi}{3}\left\{ \frac{a_1 b_1 (c_1 - z_1)^2 (2c_1 + z_1)}{c_1^2} + \frac{a_2 b_2 (c_2 - z_2)^2 (2c_2 + z_2)}{c_2^2} \right\}. \tag{11}$$

2.1. Derivation of Delay Statistics

The scatterers responsible for contribution towards a certain delay τ are located on the surface of ellipsoid ξ_τ. The commutative distribution function (CDF) is defined as the probability that a scatterer is placed inside the virtual bounding ellipsoid ξ_τ corresponding to a certain delay τ. For uniformly distributed scatterers, the CDF of ToA can be calculated from the ratio of, the volume of overlap scattering regions with virtual bounding ellipsoid V_τ, to the composite volume of whole scattering region V, [14]. The ToA CDF can thus be expressed as,

$$F_\tau(\tau) = \frac{V_\tau(\tau)}{V_{\tau_{\max}}}. \tag{12}$$

The PDF of ToA can thus be calculated by taking differential of $F_\tau(\tau)$ with respect to delay τ, which is given as below,

$$p(\tau) = \frac{\mathrm{d}}{\mathrm{d}\tau} F_\tau(\tau). \tag{13}$$

The power delay profile (PDP) gives the intensity of a signal received through a multipath channel as a function of time delay. The PDP can be calculated from PDF of ToA as below,

$$P_r(\tau) = p(\tau)\, V_{\tau_{\max}}\, P_o \left(\frac{c\,\tau}{d_{\mathrm{LoS}}}\right)^{-n}, \tag{14}$$

where, P_o is the power received by the LoS path. The Root Mean Square (RMS) Delay Spread (DS), (σ_{rms}), is the square root of the second central moment of the PDP, $P_r(\tau)$, which is given below,

$$\sigma_{\mathrm{rms}} = \sqrt{\frac{\sum P_r(\tau)\tau^2}{\sum P_r(\tau)} - \left(\frac{\sum P_r(\tau)\tau}{\sum P_r(\tau)}\right)^2}. \tag{15}$$

2.2. Derivation of Angular Statistics

The expressions for the joint and marginal PDF of AoA for the proposed generalized 3-D channel model are derived below. The Joint density function as a function of angles seen at N_2 can be found as,

$$p\left(\rho, \phi_2, \beta_2\right) = \left. \frac{f\left(\mathrm{x}_2, \mathrm{y}_2, \mathrm{z}_2\right)}{\mid J\left(\mathrm{x}_2, \mathrm{y}_2 . \mathrm{z}_2\right) \mid} \right|_{\substack{\mathrm{x}_2 = \rho\cos\beta_2 \sin\phi_2 \\ \mathrm{y}_2 = \rho\cos\beta_2\cos\phi_2 \\ \mathrm{z}_2 = \rho\sin\beta_2}}, \tag{16}$$

where the Jacobean transformation $J(\mathrm{x}_2, \mathrm{y}_2, \mathrm{z}_2)$ can be found as,

$$J\left(\mathrm{x}_2, \mathrm{y}_2, \mathrm{z}_2\right) = \frac{1}{\rho^2 \cos\beta_2}. \tag{17}$$

When the scatterers are uniformly distributed with in the defined scattering region with volume $V_{\tau_{\max}}$, the scatterer density function can be written as,

$$f\left(\mathrm{x}_2, \mathrm{y}_2, \mathrm{z}_2\right) = \begin{cases} \dfrac{1}{V_{\tau_{\max}}} & ; \quad (\mathrm{x}_2, \mathrm{y}_2, \mathrm{z}_2) \in \mathrm{ESR} \\ 0 \quad ; & \text{otherwise.} \end{cases} \tag{18}$$

Substituting (17) and (18) in (16), the joint density function can be rewritten as,

$$p\left(\rho, \phi_2, \beta_2\right) = \frac{\rho^2 \cos\beta_2}{V_{\tau_{\max}}}. \tag{19}$$

The joint PDF of AoA for azimuth and elevation angles can be found by integrating (19) over ρ for appropriate limits. The closed-form expression of joint PDF of AoA for different partitions can be written in simplified form as

below,

$$p\left(\phi_2,\beta_2\right)=\begin{cases}\frac{\left(\min(\rho_2,\rho_\tau)\right)^3\ \cos\beta_2}{3V_{\tau\max}} \\ \quad ;\pi/2>\beta_2>\beta_{t1}\text{or }\beta_{t3}>\beta_2>\beta_{t4} \\ \frac{\left(\min(\rho_2,\rho_\tau)+\min(\rho^+_{\beta_2},\rho_\tau)-\rho^+_{\beta_1}\right)^3\cos\beta_2}{3V_{\tau\max}} \\ \quad ;\ \beta_{t1}>\beta_2>\beta_{t2} \\ \frac{\left(\min(\rho_2,\rho_\tau)+\min(\rho_e,\rho_\tau)-\rho^+_{\beta_1}\right)^3\cos\beta_2}{3V_{\tau\max}} \\ \quad ;\ \beta_{t2}>\beta_2>\beta_{t3} \\ \frac{\left(\min(\rho_2,\rho_\tau,\rho_e)\right)^3\ \cos\beta_2}{3V_{\tau\max}} \\ \quad ;\ \beta_{t4}>\beta_2>-\pi/2.\end{cases} \tag{20}$$

The marginal PDF of elevation AoA is found by integrating (20) over ϕ_2 for appropriate limits, as given below,

$$p\left(\beta_2\right)=\int_{\phi_{t1}}^{\phi_{t2}}p\left(\phi_2,\beta_2\right)\mathrm{d}\phi_2\ . \tag{21}$$

Similarly, the marginal PDF of azimuth AoA is found by integrating (20) over β_2 for appropriate limits, as given belwo,

$$p\left(\phi_2\right)=\int_{\beta_{\min}}^{\beta_{\max}}p\left(\phi_2,\beta_2\right)\mathrm{d}\beta_2\ . \tag{22}$$

The derivations of parameters $\rho_e,\rho_2,\rho_\tau,\rho^+_{\beta_1},\rho^+_{\beta_2}$ and azimuth and elevation threshold angles $\phi_{t1},\phi_{t2},\beta_{t1}...\beta t4$ can be seen in next sub-section.

The multipath shape factors (SFs) proposed in [11] and [12] are notable quantifiers to measure the spread of 2-D and 3-D angular data, respectively. Fourier coefficients are used to compute SFs for analyzing the PDF of AoA. The κ^{th} complex trigonometric moment of any angular distribution is $\bar{R}_\kappa$. For example, for $p(\alpha)$, (i.e., where α may be ϕ or β for azimuthal and elevational AoA), whose total power is equal to $P_o=\int_{\alpha_{\min}}^{\alpha_{\max}}p(\alpha)\mathrm{d}\alpha$, $\bar{R}_\kappa$ is defined as,

$$\bar{R}_\kappa=\frac{1}{P_o}\int_{\alpha_{\min}}^{\alpha_{\max}}p(\alpha)\ \exp(j\alpha_\kappa)\mathrm{d}\alpha. \tag{23}$$

Only first and second moments are used in characterization of the SFs. $|\bar{R}_1|$ is the magnitude of first trigonometric moment. The SF angular spread, Λ_α, is given as below,

$$\Lambda_\alpha=\sqrt{1-|\bar{R}_1|^2}. \tag{24}$$

The angular spread SF measures the spread with a value between 0 and 1. A value close to 0 indicate that signals from a wider range of angles are received and a value close to 1 indicate a sharp angular spread. The other important SF angular constriction, γ_α, is defined as below,

$$\gamma_\alpha=\frac{|\bar{R}_2-\bar{R}_1^2|}{1-|\bar{R}_1|^2}. \tag{25}$$

The angular constriction shape factor measures the bias of angular data towards exactly two physical directions. A value 1 indicates the extreme case of signals arriving exactly from two physical directions, and a value 0 indicate no bias towards two directions.

2.3. Derivation of Angular Partitions

A cross-section view of the scattering region for a certain azimuth and elevation angle of observation at node N_2 is shown in Fig. 2. The vertical distance from the origin of E_1 to the antenna of N_1 is denoted by $h_{e1}=h_1-z_1$. Similarly, the vertical distance from the origin of E_2 to the antenna of N_2 is shown by $h_{e2}=h_2-z_2$. The difference between the elevation of the origin of E_1 and antenna of N_2 is shown by $h_{e3}=h_2-z_1$. Similarly, the difference between the elevation of the origin of E_2 and antenna of N_1 is shown by $h_{e4}=h_1-z_2$. A line originated from the node N_2 in the direction of observation (given, ϕ_2 and β_2) intersects E_2 at point ς_2, E_1 at points ς_1 and ς_1', and ξ_τ at point ς_τ; the distance from N_2 to these intersection points is denoted by ρ_2, $\rho^+_{\beta 1}$ and $\rho^-_{\beta 2}$, and ρ_τ, respectively. Mathematical expressions for these distances can be obtained by substituting the equation of the line into the equation of respective ellipsoid (E_1, E_2, or ξ_τ) and solving for the radial distance. After performing tedious mathematical simplifications, the expression for ρ_2, $\rho^+_{\beta 1}$, $\rho^-_{\beta 2}$, and ρ_τ are derived as given below,

$$\begin{aligned}\rho_2=&\frac{1}{2a_2^2b_2^2+c_2^2(a_2^2+b_2^2)-c_2^2\Psi-\left(2a_2^2b_2^2-c_2^2(a_2^2+b_2^2)\right)\cos(2\beta_2)}\times\\&\Big\{4a_2^2b_2^2h_{e2}\sin\beta_2-2\Big(a_2^2b_2^2c_2^2\Big(b_2^2(c_2^2-h_{e2}^2)\\&+a_2^2(2b_2^2+c_2^2-h_{e2}^2)-\Psi(c_2^2-h_{e2}^2)+\Big(b_2^2(c_2^2-h_{e2}^2)\\&+a_2^2(-2b_2^2+c_2^2-h_{e2}^2)\Big)\cos(2\beta_2)\Big)\Big)^{1/2}\Big\},\end{aligned} \tag{26}$$

DOI: 10.1002/ett
Prepared using ettauth.cls

$$\left.\begin{matrix}\rho^{+}_{\beta 1}\\ \rho^{-}_{\beta 2}\end{matrix}\right\} = \frac{-1}{a_\phi^2 + c_\phi^2 + (c_\phi^2 - a_\phi^2)\cos(2\beta_2)} \times \left\{ -2c_\phi^2\, \rho_{e2} \cos\beta_2 - 2h_{e3}\, a_\phi^2 \sin\beta_2 \pm \left(2a_\phi^2 c_\phi^2 \times \left(a_\phi^2 + c_\phi^2 - h_{e3}^2 - \rho_{e2}^2 - \left(a_\phi^2 - c_\phi^2 + h_{e3}^2 - \rho_{e2}^2\right) \cos(2\beta_2) + 2h_{e3}\, \rho_{e2} \sin(2\beta_2) \right) \right)^{1/2} \right\}, \tag{27}$$

$$\rho_\tau = \left\{ -5a_\tau^2 - 3b_\tau^2 + (a_\tau^2 - b_\tau^2)\Big(-\cos(2\beta_{\mathrm{LoS}}) + \cos(2\beta_2)\big(-1 + 3\cos(2\beta_{\mathrm{LoS}})\big) + 4\cos^2\beta_2 \cos^2\beta_{\mathrm{LoS}} \cos(2\phi_2) - 4\cos\phi_2 \sin(2\beta_2)\sin(2\beta_{\mathrm{LoS}})\Big) \right\}^{-1} \times \left\{ -4b_\tau^2 d_{\mathrm{LoS}} \cos\beta_2 \cos\beta_{\mathrm{LoS}} \cos\phi_2 + 4b_\tau^2 d_{\mathrm{LoS}} \sin\beta_2 \sin\beta_{\mathrm{LoS}} - \left(2a_\tau^2 b_\tau^2 \left(20a_\tau^2 + 12b_\tau^2 - 5d_{\mathrm{LoS}}^2 + (4a_\tau^2 - 4b_\tau^2 - d_{\mathrm{LoS}}^2) \Big(\cos(2\beta_2)\big(1 - 3\cos(2\beta_{\mathrm{LoS}})\big) + \cos(2\beta_{\mathrm{LoS}}) - 4\cos^2\beta 2 \cos^2\beta_{\mathrm{LoS}} \cos(2\phi_2) + 4\cos\phi_2 \sin(2\beta_2)\sin(2\beta_{\mathrm{LoS}})\Big) \right) \right)^{1/2} \right\}, \tag{28}$$

where the parameters Ψ, a_ϕ, c_ϕ, and ρ_{e2} are the geometric simplification parameters. Ψ can be expressed as given below,

$$\Psi = 2(a_2^2 - b_2^2)\cos^2\beta_2\ \cos(2\theta_2 - 2\phi_2). \tag{29}$$

The parameters a_ϕ and c_ϕ are the major and minor dimensions of a vertical 2-D ellipse ε_ϕ formed at the vertical cross-section of ellipsoid E_1 for a certain given azimuth angle (ϕ_2) observed at N_2.

$$a_\phi = \frac{\sec\phi_2}{a_1^2 + b_1^2 + (b_1^2 - a_1^2)\cos(2\theta_1 - 2\phi_2)} \times \left\{ -2a_1^2 b_1^2 \cos^2\phi_2 \big(d^2 - a_1^2 - b_1^2 + (a_1^2 - b_1^2)\cos(2\theta_1 - 2\phi_2) - d^2\cos(2\phi_2)\big) \right\}^{1/2} \tag{30}$$

$$c_\phi = c_1 \times \sqrt{\frac{-b_1^2\rho_{e1}^2 + a_1^2(2b_1^2 - \rho_{e1}^2) + (a_1^2 - b_1^2)\rho_{e1}^2\cos(2(\theta_1 + \phi_e))}{2a_1^2 b_1^2}}, \tag{31}$$

where the parameter ϕ_e can be obtained as,

$$\phi_e = \arcsin\left(\frac{\rho_{e2}\sin\phi_2}{\rho_{e1}}\right). \tag{32}$$

The origin of the vertical 2-D ellipse ε_ϕ is labeled as w_ϕ in Fig. 2. The horizontal distance from N_1 and N_2 to the point w_ϕ is denoted by ρ_{e1} and ρ_{e2}. These distances can be obtained as,

$$\rho_{e1} = \sqrt{d^2 + \rho_{e2}^2 - 2d\ \rho_{e2}\ \cos\phi_2}, \tag{33}$$

$$\rho_{e2} = -d\ \frac{(a_1^2 - b_1^2)\cos(2\theta_1 - \phi_2) - (a_1^2 + b_1^2)\cos\phi_2}{a_1^2 + b_1^2 + (b_1^2 - a_1^2)\cos(2\theta_1 - 2\phi_2)}. \tag{34}$$

The length of line drawn from N_2 to the intersection points on ellipse ε_ϕ at an elevation of z_1 is denoted by $\rho^{+}_{\phi 1}$ and $\rho^{-}_{\phi 2}$. The simplified solution can be expressed as,

$$\left.\begin{matrix}\rho^{+}_{\phi 1}\\ \rho^{-}_{\phi 2}\end{matrix}\right\} = \frac{-1}{a_1^2 + b_1^2 + (b_1^2 - a_1^2)\cos(2\theta_1 - 2\phi_2)} \times \left\{ \sec\phi_2 \left(2\, a_1^2\, b_1^2 \cos^2\phi_2 \times \left(a_1^2 + b_1^2 - d^2 + (b_1^2 - a_1^2)\cos(2\theta 1 - 2\phi_2) + d^2\cos(2\phi_2)\right)\right)^{1/2} - 2d\big(b_1^2\cos\theta_1\cos(\theta_1 - \phi_2) + a_1^2\sin\theta_1\ \sin(\theta_1 - \phi_2)\big) \right\}. \tag{35}$$

Similarly, the length of line from N_2 to the intersection points with ε_ϕ formed at any arbitrary elevation z can be obtained by replacing the dimensions a_1 and b_1 with $a_{1,z}$ and $b_{1,z}$ in the above equation. The parameters $a_{1,z}$ and $b_{1,z}$ represent the major and minor dimensions of the horizontal cross-section of E_1 formed at an height z; which can be expressed as,

$$a_{1,z} = \frac{a_1\sqrt{c_1^2 - (z - z1)^2}}{c_1}, \tag{36}$$

$$b_{1,z} = \frac{b_1\sqrt{c_1^2 - (z - z1)^2}}{c_1}. \tag{37}$$

Azimuth threshold angles to differentiate among the angular regions of different geometrical composition of the ESR are illustrated in Fig. 3. The azimuth angles observed at N_2 in the horizontal plane at an height z_1 (i.e., for maximum horizontal cross-section of E_1) are labeled

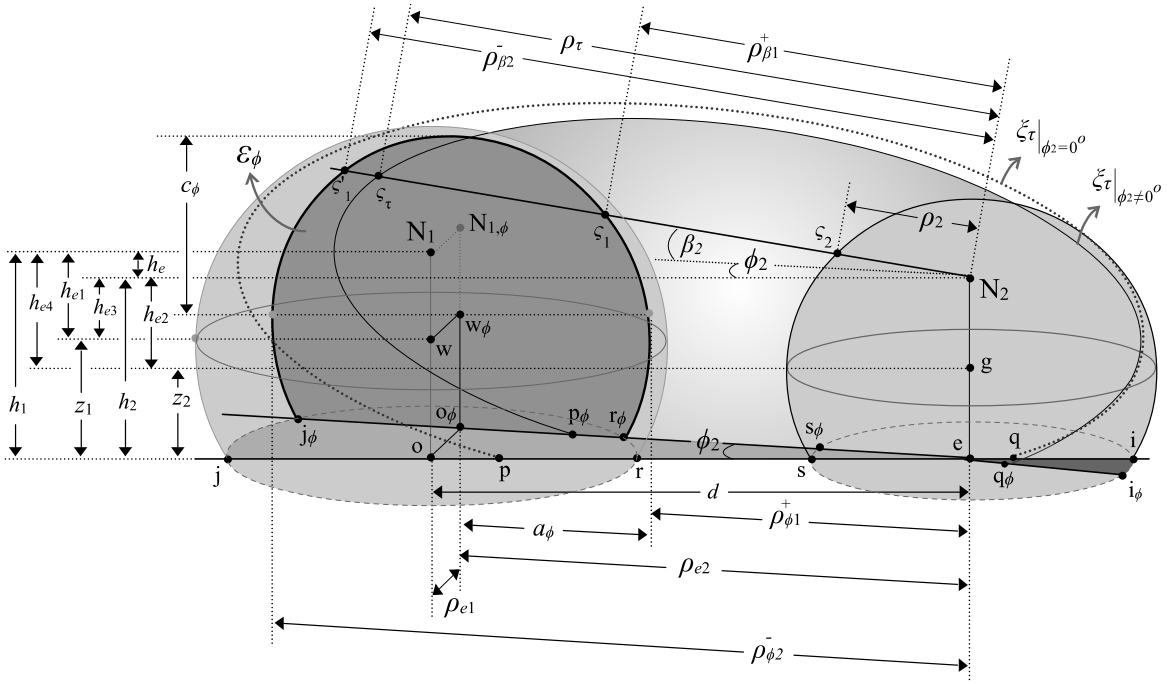

Figure 2: Cross-section view of the proposed model for a fixed direction of observation in azimuth and elevation planes from node N_2.

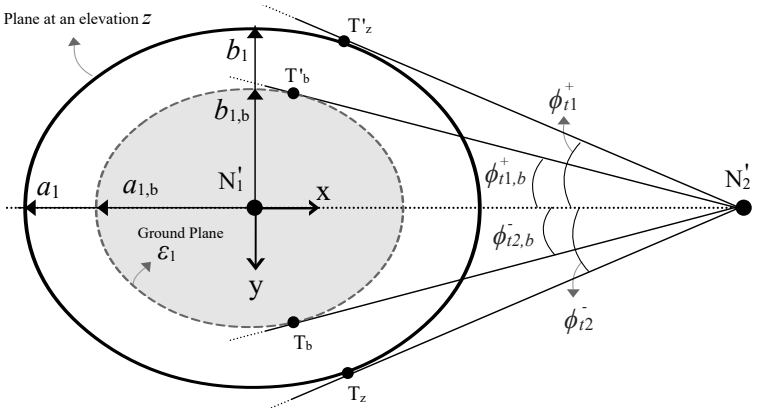

Figure 3: Top-view (x-y plane) of the proposed model with azimuth threshold angle observed from N_2.

by ϕ^+_{t1} and ϕ^-_{t2}. These angles are subtended by the lines originated from N'_2 (projection of N_2 at a certain elevation z) to the tangent points T_z and T'_z, see Fig. 3 at the surface of E_1 for an elevation $z = z_1$. Simplified mathematical expression for these angles can be expressed as given below,

$$\left.\begin{matrix}\phi^+_{t1}\\ \phi^-_{t2}\end{matrix}\right\} = \arctan\Bigg(\frac{1}{d^2 - a_1^2\cos^2\theta_1 - b_1^2\sin^2\theta_1}\times \Big\{(b_1^2 - a_1^2)\cos\theta_1\sin\theta_1 \pm\sqrt{b_1^2d^2\cos^2\theta_1 + a_1^2(-b_1^2 + d^2\sin^2\theta_1)}\Big\}\Bigg). \tag{38}$$

Similarly, the azimuth threshold angles formed at any arbitrary elevation z can be obtained by replacing the

DOI: 10.1002/ett
Prepared using ettauth.cls

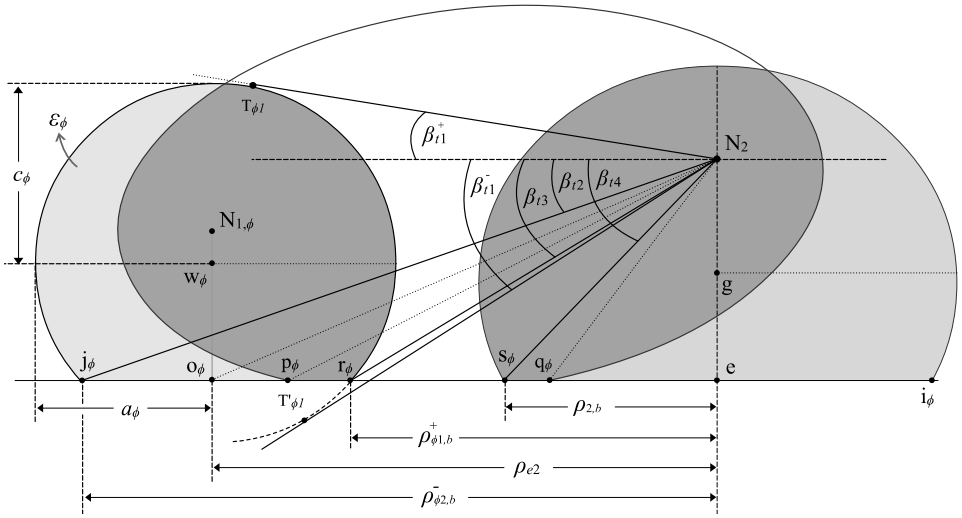

Figure 4: Side-view (x-z plane) of the proposed model, indicating elevation threshold angles observed from N_2 for a fixed azimuth angle of observation ϕ_2.

dimensions a_1 and b_1 with $a_{1,z}$ and $b_{1,z}$ in the above equation. The dimensions of the 2-D ellipse (ε_1) formed with the cross-section of scattering ellipsoids, E_1, and the ground plane can also be obtained from (36) and (37) by setting $z = -z_1$. Subsequently, the azimuth threshold angles ($\phi_{t1,b}^{+}$ and $\phi_{t2,b}^{-}$, see Fig. 3) formed at the ground plane can be deduced from (38) by substituting $a_1 = a_{1,z}$ and $b_1 = b_{1,z}$ with $z = -z1$.

Important elevation threshold angles, to differentiate among the angular regions based upon their geometrical composition, are illustrated in Fig. 4. The elevation threshold angles subtended by a line drawn at a certain fixed azimuth angle ϕ_2 from N_2 to the tangent points $T_{\phi 1}$ and $T'_{\phi 1}$ at the vertical ellipse ε_ϕ are denoted by β_{t1}^{+} and β_{t1}^{-}; these angles can be expressed as,

$$\left.\begin{matrix}\beta_{t1}^{+}\\ \beta_{t1}^{-}\end{matrix}\right\} = \begin{cases} \arctan\left(\frac{-h_{e3}\rho_{e2} \pm \sqrt{a_\phi^2 h_{e3}^2 + c_\phi^2(-a_\phi^2+\rho_{e2}^2)}}{\rho_{e2}^2 - a_\phi^2}\right) \\ \qquad ; \phi_{t2}^{-} \le \phi_2 \le \phi_{t1}^{+} \\ 0 \qquad ; \text{ otherwise} \end{cases} \tag{39}$$

The intersection points of vertical 2-D ellipse ε_ϕ and ground plane are labeled by j_ϕ and r_ϕ, see Fig. 4. The angles formed with the line drawn from N_2 to these intersection points are denoted by β_{t2} and β_{t3}, which can be expressed as given below,

$$\beta_{t2} = \begin{cases} \arctan\left(\frac{h_2}{\rho_{\phi 2,b}^{-}}\right) & ; \ \phi_{t2}^{-} \le \phi_2 \le \phi_{t1}^{+} \\ 0 & ; \text{ otherwise,} \end{cases} \tag{40}$$

$$\beta_{t3} = \begin{cases} \arctan\left(\frac{h_2}{\rho_{\phi 1,b}^{+}}\right) & ; \ \phi_{t2}^{-} \le \phi_2 \le \phi_{t1}^{+} \\ 0 & ; \text{ otherwise.} \end{cases} . \tag{41}$$

Similarly, the elevation angle formed with the intersection point s_ϕ of the vertical slice of scattering region around N_2 with the ground plane is denoted by β_{t4}, which is given as under,

$$\beta_{t4} = \arctan\left(\frac{h_2}{\rho_{2,b}}\right), \tag{42}$$

where the parameter $\rho_{\phi 1,b}^{+}$ and $\rho_{\phi 2,b}^{-}$ represent the horizontal distance from N_2 to the intersection points r_ϕ and j_ϕ, recall Fig. 4. These parameters can be obtained from (35) by substituting $a_1 = a_{1,z}$, $b_1 = b_{1,z}$, and $z = -z_1$.

3. RESULTS AND DISCUSSIONS

This section presents the obtained analytical results on delay and angular characteristics of the channel. A thorough analysis on the impact of various physical channel

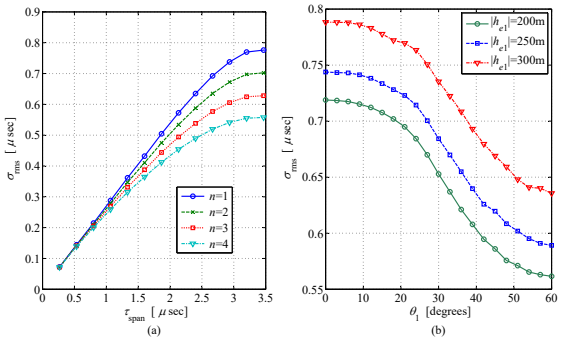

Figure 5: Trend of Delay Spread w.r.t. physical channel parameters. (a) Relationship between delay-span and RMS-DS for different values of path-loss exponent, ($a_1 = a_2$ = 500m, $b_1 = b_2$ = 250m, $c_1 = c_2$ = 175m, $h_1 = h_2$ = 0m, $z_1 = z_2$ = 0m, d = 1000m, $\theta_1 = 0^o$, $\theta_2 = 0^o$). (b) Impact of the orientation of scattering volume and vertical spatial deviation of mobile node from the center of scattering volume, ($a_1 = a_2$ 500m, $b_1 = b_2$ = 250m, $c_1 = c_2$ = 200m, h_2 = 0m, z_2 = 200m, d = 1000m, $\theta_2 = 0^o$, $\tau_{\max}$ = 6.74 μsec).

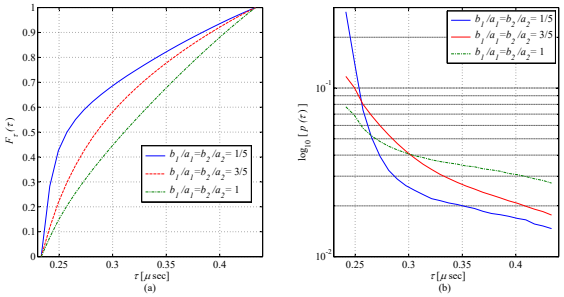

Figure 6: The impact of transformation of scattering volumes from spherical to ellipsoidal shape on the CDF and PDF of ToA, shown in (a) and (b), respectively, (c_1 = 10m, c_2 = 20m, $h_1 = h_2$ = 10m, $z_1 = z_2$ = 10m, d = 70m, $\theta_1 = \theta_2 = 0^o$, $\tau_{\max}$ = 0.43 μsec).

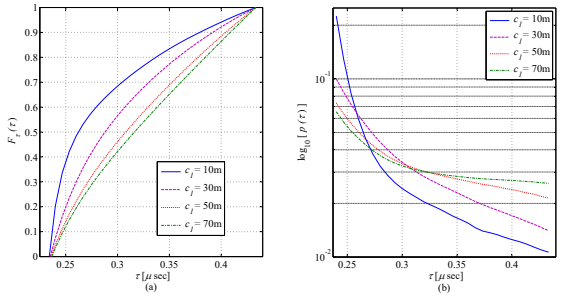

Figure 7: The impact of increase in the amount of scattering objects along the elevation axis in the vicinity of far-end communicating node on the CDF and PDF of ToA, shown in (a) and (b), respectively. ($a_1 = a_2$ 50m, b_1 = 25m, b_2 = 30m, c_2 = 20m, $h_1 = h_2$ = 10m, $z_1 = z_2$ = 10m, d = 70m, $\theta_1 = \theta_2 = 0^o$, $\tau_{\max}$ = 0.43 μsec).

parameters on statistical characteristics of multipath signals in delay and angular domains is presented.

3.1. Delay Statistics

The spread of multipath signals in the delay domain leads to frequency selectivity of the channel. The measure of delay-span alone is not sufficient to provide realistic picture of multipath delay spread; therefore, it is necessary to consider both the delay-span and the peak(s) of the ToA distribution to quantify the delay spread. The definition of RMS-DS is the most favorable quantifier in the literature to gauge the spread of multipath waves in delay domain. The relationship between delay-span and RMS-DS for the proposed channel model is demonstrated in Fig. 5 (a), where the impact of path-loss exponent is also shown. The values of the parameters taken for the graphs are indicated in caption of the relevant figures. The RMS-DS of the multipath energy decreases nonlinearly with a decrease in delay-span, and it decreases sharply for the smaller values of the span. In Fig. 5 (b), the impact of vertical spatial deviation of mobile node from the center of scattering volume (i.e., h_{e1}) and horizontal orientation of scattering volume (i.e., θ_1) on the RMS-DS of the channel is shown.

Circular or elliptical shaped scattering region in the vicinity of a mobile node is usually considered better approximation of the physical reality to model sparsely populated small towns or dense urban streets, respectively. The shape of the scattering region changes in accordance with the terrain, clutter, and spatial position of scattering structures in the vicinity of communication nodes; therefore, fixing the geometric shape of the scattering volumes to be either spherical or ellipsoidal alone and fixing the position of antennas in the center of scattering volumes, does not allow full flexibility to the physical channel modeling. The proposed model is thus designed tunable in its geometric parameters to more realistically adapt the physical environment. The impact of transforming the scattering volumes around both the ends of the communication link from circular shape to elliptical shape (changing eccentricity of ellipsoids) in horizontal plane on ToA distribution characteristics are shown in Fig. 6. With a decrease in the ratio between minor

DOI: 10.1002/ett
Prepared using ettauth.cls

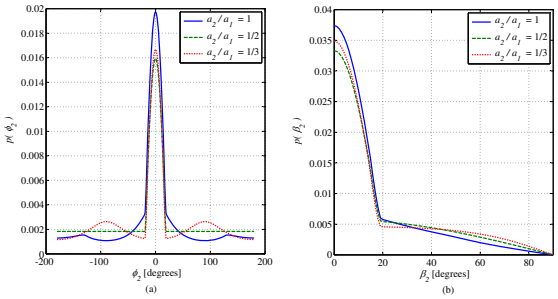

Figure 8: The impact of tuning the ratio between the dimensions of major axes of the scattering ellipsoids around both the ends of the communication link on the PDF of azimuth AoA and elevation AoA, shown in (a) and (b), respectively. (b_1 = 20m, c_1 = 20m, b_2 = 15m, c_2 = 15m, $h_1 = h_2$ = 0m, $z_1 = z_2$ = 0m, d = 65m, $\theta_1 = \theta_2 = 0^o$, $\tau_{\max}$ = 0.32 μsec).

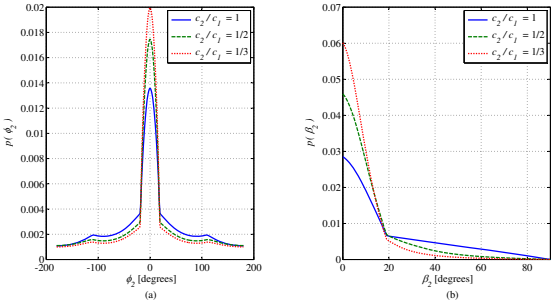

Figure 9: The impact of tuning the ratio between the dimensions of minor axes of the scattering ellipsoids around observing- and far-ends of the communication link on the PDF of azimuth AoA and elevation AoA, shown in (a) and (b), respectively. ($a_1 = a_2$ = 30m, $b_1 = b_2$ = 20m, $h_1 = h_2$ = 0m, $z_1 = z_2$ = 0m, d = 65m, $\theta_1 = \theta_2 = 0^o$, $\tau_{\max}$ = 0.32 μsec).

and major axes of scattering volumes, the probability of arrival of signal from the directions around LoS direction increases, which further increases the probability of arrival of signal with shorter delays. In the emerging next-generation wireless communication networks, the decrease in elevation of BS and size of cells in dense urban propagation environments, make it necessary to accurately model the spatial location of scattering objects in both elevation and azimuth plane. The effect of increasing the amount of scattering objects along elevation axis on distribution of ToA is shown in Fig. 7. Only the local scattering objects around a mobile node in rural areas (typical macro-cellular environment) correspond in the arrival of multipath signals; where the high elevation of BS makes the vicinity of BS a scattering free region. On the other hand, in densely populated and low BS antenna height outdoor and indoor environments (i.e., micro-cellular and pico-cellular), the effective scatterers are concentrated around both the ends of the link.

3.2. Angular Statistics

It is observed that the change in scattering volume around the observing-end changes the tails of AoA distribution and change in the scattering volume around observing-end impacts the AoA distribution for the directions around LoS path. The impact of changing the relative volume of independent scattering regions around both the communicating nodes on the PDF of azimuth and elevation AoA is shown in Fig. 8. The impact of relative amount of scatterers in the elevation plane around both the ends

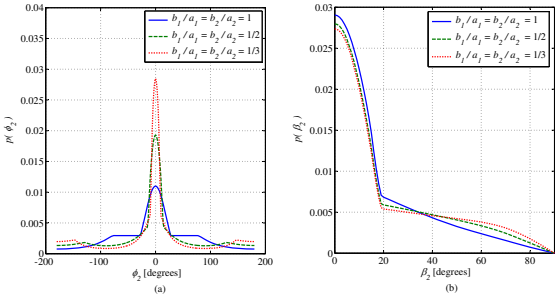

Figure 10: The impact of transformation of scattering volumes from spherical to ellipsoidal shape on the PDF of azimuth AoA and elevation AoA shown in (a) and (b), respectively. ($c_1 = c_2$ = 20m, $h_1 = h_2$ = 0m, $z_1 = z_2$ = 0m, d = 65m, $\theta_1 = \theta_2 = 0^o$, $\tau_{\max}$ = 0.32 μsec).

of the link on the PDF of azimuth and elevation AoA is shown in Fig. 9. The increase in ratio of c_1/c_2 means an increase in the volume of scattering region around the far-end node with respect to the observing-end. It can be seen that values of the PDF of azimuth AoA increases along the LoS direction with an increase in ratio of c_1/c_2 and it shows converse behavior for tails of the distribution for the angles away from LoS direction. The elevational angular spread is observed to increase with a decrease in ratio c_1/c_2, which indicates that the local scattering objects in elevation plane around the observing-end has higher influence on the elevational AoA distribution compared to the scatterers in elevation plane around the far-end. The impact of transforming the scattering volumes around both the ends of the communication link from circular shape to elliptical shape (changing eccentricity of ellipsoids)

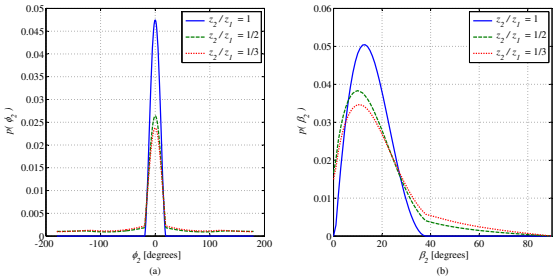

Figure 11: The impact of tuning vertical positions of the (origins of) scattering ellipsoids on the PDF of azimuth AoA and elevation AoA, shown in (a) and (b), respectively.($a_1 = a_2$ = 30m, $b_1 = b_2$ = 20m $c_1 = c_2$ = 20m, $h_1 = h_2$ = 0m, d = 65m, $\theta_1 = \theta_2 = 0^o$, $\tau_{\max}$ = 0.32 μsec).

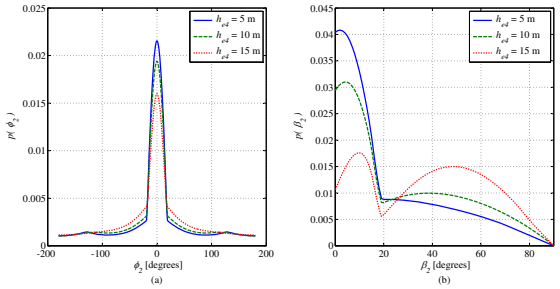

Figure 12: The impact of vertical displacement of (origin of) scattering volume around observing-end w.r.t. the position of far-end antenna on the PDF of azimuth AoA and elevation AoA, shown in (a) and (b), respectively.(a_1 = 30m, b_1 = 30m, c_1 = 30m, a_2 = 25m, b_2 = 15m, c_2 = 15m, h_2 = 0m, z_1 = 0m, d = 65m, $\theta_1 = \theta_2 = 0^o$, $\tau_{\max}$ = 0.32 μsec).

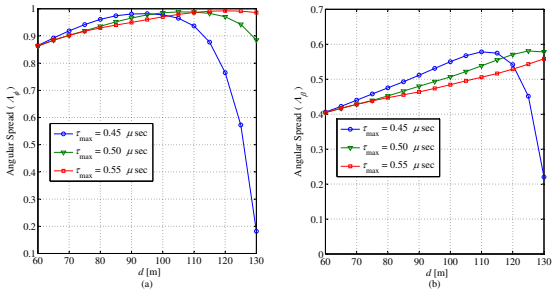

Figure 13: The impact of change in delay span and horizontal distance between communicating nodes on the angular spread in azimuth and elevation plane shown in (a) and (b), respectively.(a_1 = 30m, b_1 = 20m, c_1 = 20m, a_2 = 25m, b_2 = 15m, c_2 = 15m, h_1 = 30m, h_2 = 0m, z_1 = 5m, z_2 = 0m, $\theta_1 = \theta_2 = 0^o$).

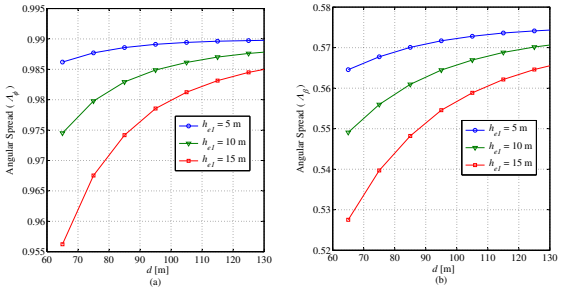

Figure 14: The impact of change in horizontal distance between communicating nodes and vertical displacement of (the origin of) observing-end's scattering ellipsoid w.r.t. the height of far-end's antenna on angular spread observed in azimuth and elevation planes, shown in (a) and (b), respectively.(a_1 = 30m, b_1 = 20m, c_1 = 20m, a_2 = 25m, b_2 = 15m, c_2 = 15m, h_2 = 0m, z_2 = 0m, $\theta_1 = \theta_2 = 0^o$).

in horizontal plane on AoA distribution characteristics are shown in Fig. 10. With a decrease in the ratio between minor and major axes of scattering volumes, the probability of arrival of signal from the directions around LoS direction increases, which further increases the probability of arrival of signal with shorter delays. The impact of change in the ratio between the height of origins of scattering volumes around both the ends of the communication link on the PDF of AoA in azimuth and elevation planes is shown in Fig. 11 (a) and (b), respectively. This graph is left non-normalized, in order to clearly present the effect of the ratio. It can be observed that with an increase in the ratio z_1/z_2, the PDF of azimuth AoA becomes sharper along the LoS direction and tails of the PDF also become prominent. On the other hand, with a change in z_1/z_2 the peak of elevation AoA PDF shifts along elevation axis however the shape of the PDF remains similar. This indicates the importance of inclusion of scatterers in the elevation plane while modeling the scattering region. The effect of vertical deviation of the scattering volume around the observing-end node (i.e., N_2) with respect to the elevation of antenna of far-end node on the PDF of azimuth and elevation AoA is shown in Fig. 12 (a) and (b), respectively. With an increase in h_{e4}, the PDF of azimuth AoA becomes prominent along LoS direction and angular spread decreases. In elevation plane, with a decrease in h_{e4}, the tails of the PDF (for $\beta_2 > 20^o$) become significantly prominent and thus the angular decreases. The spatial location of the effective scattering objects in a particular propagation environment determine the angular characteristics of the multipaths arrived at the receiver. The angular spread of the mulipath

DOI: 10.1002/ett
Prepared using ettauth.cls

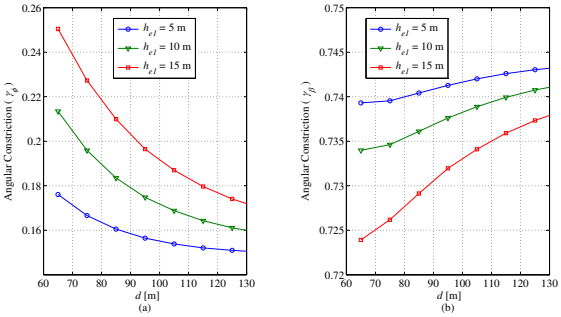

Figure 15: The impact of change in horizontal distance between communicating nodes and vertical displacement of (the origin of) far-end's scattering region w.r.t. the height of far-end's antenna on angular constriction observed in azimuth and elevation plane, shown in (a) and (b), respectively.(a_1 = 30m, b_1 = 20m, c_1 = 20m, a_2 = 25m, b_2 = 15m, c_2 = 15m, h_2 = 0m, z_2 = 0m, $\theta_1 = \theta_2 = 0^o$).

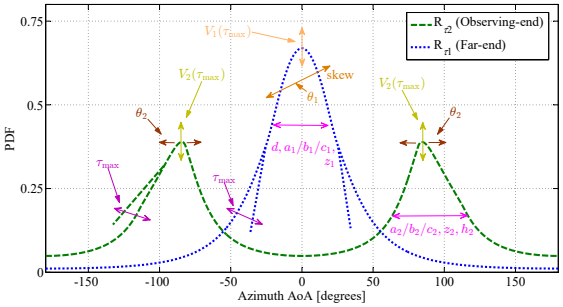

Figure 16: Summary of the influence of the proposed model's geometric parameters on PDF of azimuth AoA.

waves further determine the space, time, and frequency selective characteristics of the channel. Therefore, it is of vital importance to study the behaviour of angular spread for characterization of radio propagation channels. Various quantifier to measure the dispersion of energy in angular domain are available in the literature. The multipath shape factors theory is considered most favorable to measure the dispersion of energy in angular domain in the form of angular spread Λ and angular constriction γ. The impact of different physical channel parameters on angular spread is studied on the base of these shape factor quantifiers. The angular spread of the mutipath waves with respect to the horizontal link-distance and maximum considered excess delay is plotted in Fig. 13 (a) and (b) for azimuth Λ_ϕ and elevation Λ_β planes, respectively. The azimuthal and elevational angular spread is observed to increase gradually with an increase in the horizontal link-distance d, since increasing the link distance enhances the tails and sharpens the peak along LoS direction. However, after a certain value of link-distance the influence of the peak of the PDF along LoS direction (caused by far-end scattering volume) on the angular spread measure becomes leaner compared to the peaks in the tails of the PDF caused by local scattering volume; therefore the behaviour of angular spread reverses along link-distance axis. The trend of decrease in the angular spread for higher values of link-distance becomes sharper with a decrease in the maximum excess delay. The effect of change in vertical deviation h_{e1} of far-end scattering volume E_2 with reference to the antenna height of far-end node N_1 on angular spread and angular constriction (in both azimuth and elevation planes) with respect to horizontal link distance d is shown in Fig. 14 and Fig. 15, respectively. Both the azimuthal and elevational angular spread is observed to decrease with a decrease in link-distance, however, it decreases more sharply for higher values of the vertical deviation h_{e1}. On the other hand, the azimuthal angular constriction is observed to increase nonlinearly with a linear decrease in the link-distance and the rate of it's increase further increases with an increase in vertical deviation h_{e1}. However, the elevational angular constriction shows a converse behaviour along both the parameters d and h_{e1}. Summary of the effect of the proposed model's input parameters on the PDF of azimuth AoA discussed above is illustrated in Fig. 16. The two curves show the contribution of observing-end and far-end scattering objects in the PDF of azimuth AoA; the composite pdf of azimuth AoA can thus be obtained by adding these two.

3.3. Model Validation

3.3.1. Validation through Computer Simulations

In order to demonstrate the validity of the derived analytical expressions, computer based simulations are performed. A comparison of simulation results with analytical results obtained for the proposed model is provided in Fig. 17. Realization of effective scattering points in generated from uniform distribution limited within the defined scattering region. The results are taken for 10^3 uniformly distributed scattering points, and averaged over 10^4 monte carlo runs. A good match is observed between simulation and analytical results for all

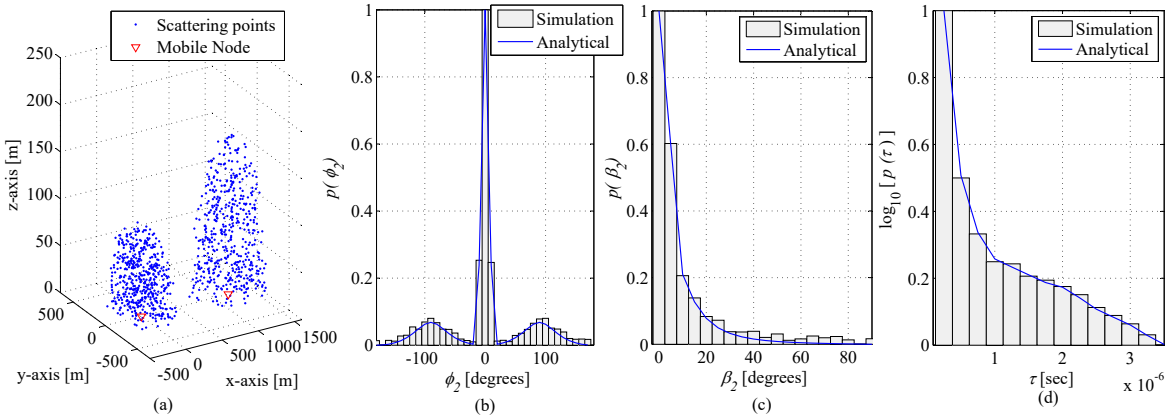

Figure 17: Comparison of simulations and analytical results. (a) Spatial distribution of scattering points taken for simulation setup, (b) PDF of azimuth AoA, (c) PDF of elevation AoA, (d) PDF of ToA. (a_1 = 300m, b_1 = 500m, c_1 = 100m, a_2 = 500m, b_2 = 250m, c_2 = 175m, d = 1200m, h_1 = 0m, h_2 = 0m, z_1=0m, z_2 = 0m, $\theta_1 = \theta_2 = 0^o$).

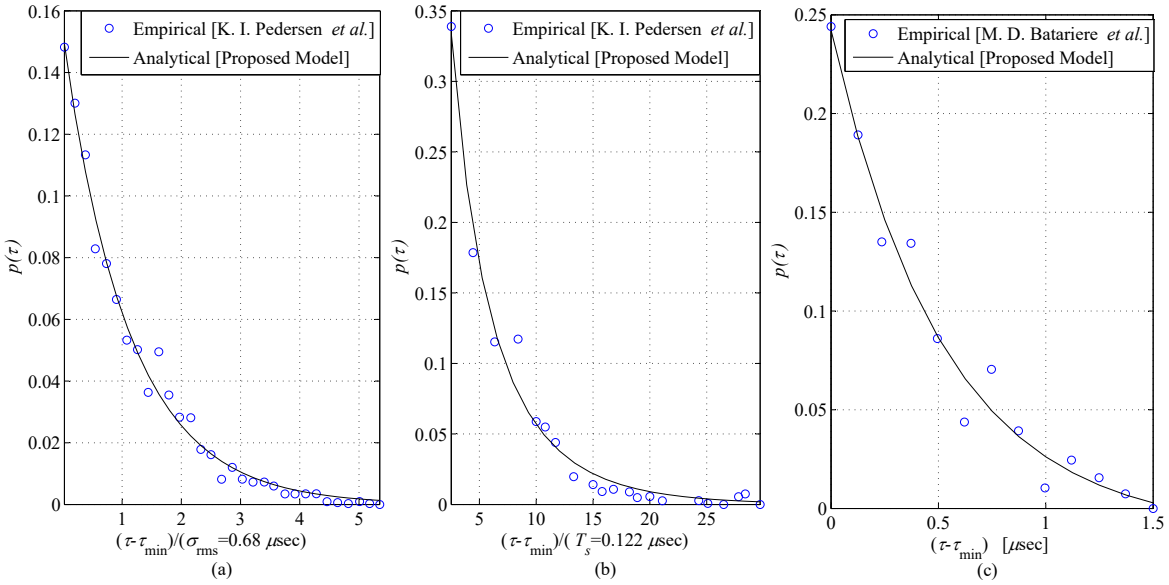

Figure 18: Curve-fitting analytical results after matching the ToA PDF obtained from the proposed model to the empirical data-sets for outdoor propagation environments in K. I. Pedersen *et al.* [20], K. I. Pedersen *et al.* [20], and M. D. Batariere *et al.* [21] shown in (a), (b), and (c), respectively.

azimuth AoA, elevation AoA, and ToA statistics of the channel.

3.3.2. Validation through Empirical Data

A detailed comparison of the proposed analytical results with empirical data-sets available in the literature is presented to demonstrate the validity of the proposed model in Fig. 18, 19, and 20 for ToA, outdoor AoA, and indoor AoA statistics, respectively. The discrete data samples of the empirical data-sets obtained for different outdoor propagation environments provided in [20, 21, 22, 23, 24, 25] are extracted through "GetData Graph Digitizer" instead of human visual reading. See http://www.getdata-graph-digitizer.com/. However, the data samples for joint ToA and azimuth AoA (at 0° elevation AoA) indoor measurement campaign results in [26] are manually extracted from the provided contour maps, by manually employing a careful color decoding through image processing tools. These joint (3D) data samples are numerically integrated over delay (τ) to obtain

DOI: 10.1002/ett
Prepared using ettauth.cls

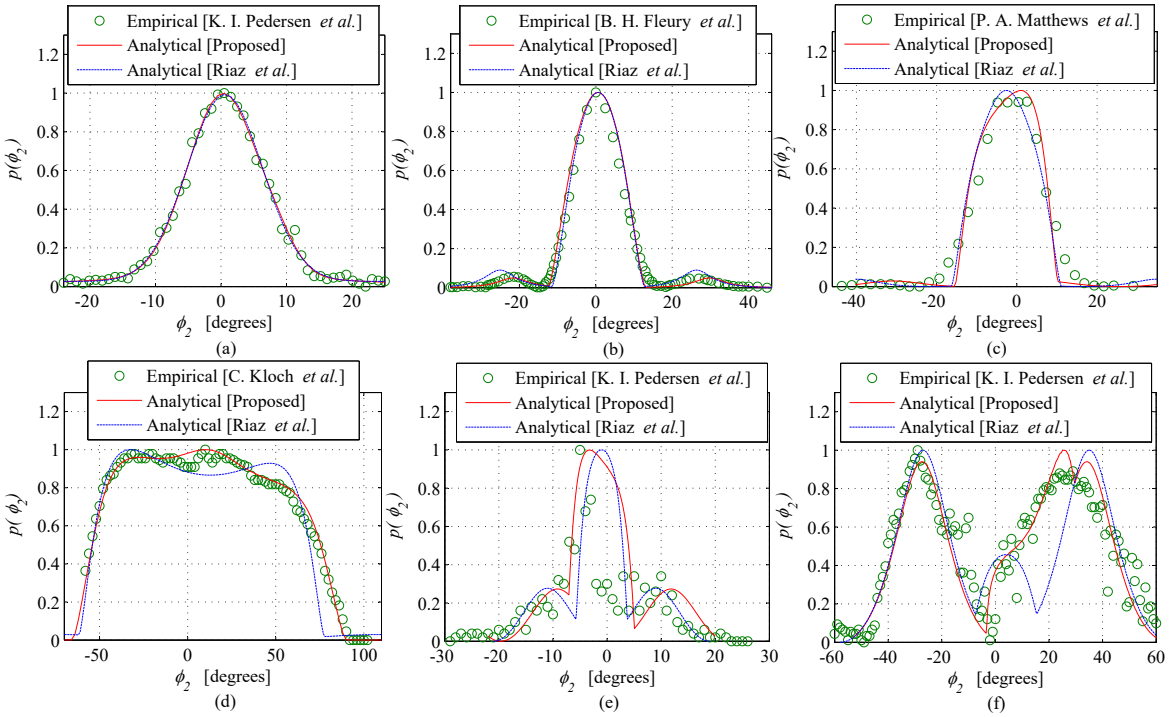

Figure 19: Curve-fitting proposed analytical results after matching the azimuth AoA PDF obtained from the proposed model to the empirical data-sets for outdoor propagation environments available in K. I. Pedersen *et al.* [20], B. H. Fleury *et al.* [22], P. A. Matthews *et al.* [23], C. Kloch *et al.* [24], K. I. Pedersen *et al.* [25], and K. I. Pedersen *et al.* [20] shown in (a), (b), (c), (d), (e), and (f), respectively.

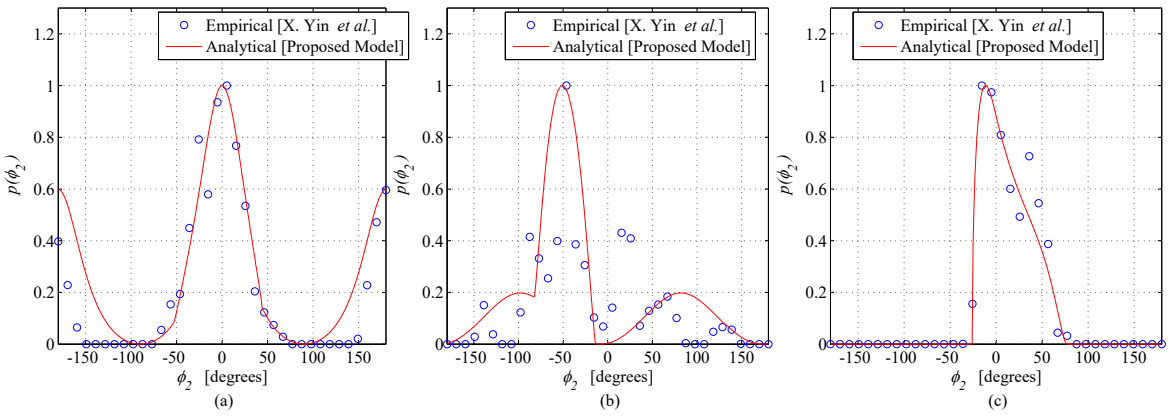

Figure 20: Curve-fitting proposed analytical results after matching the azimuth AoA PDF obtained from the proposed model to the empirical data-sets for indoor propagation environments available in X. Yin *et al.* [26] in (a) LoS measurement scenario, (b) NLoS measurement scenario 1, and (c) NLoS measurement scenario 2.

marginal PDF of azimuth AoA. All the extracted empirical data-sets for outdoor and indoor environments are scaled along vertical axis to fix their peak(s) at 1, which is performed by dividing all the values of a data-set by its peak value. The normalized data-sets and/or analytical plots obtained from proposed model are shifted (circularly) and scaled along horizontal axis to align with each other.

There are various notable methods available in the literature, see e.g., [27, 28, 29], which can be used to adopt the input geometric parameters for modeling a specific propagation environment. Considering the available details

of the targeted measurement campaigns and the knowledge of the impact of input geometric parameters on the output curves (see the summary plotted in Fig. 16), a reasonable range can be defined for the those input geometric parameters for which no direct information is available in the measurement-campaign details. The strategy used for setting the input geometric parameters of the proposed model (for comparison with measurement results) can be defined in following three steps,

1. The first category of input parameters (with directly available values in measurement-campaign details) are substituted the exact same value as in measurement campaign (e.g., link distance d, height of nodes h_m, and delay span τ_{span}).
2. For the second category of input parameters, which cannot be directly set from the measurement campaign details due to insufficient available information, a reasonable range (constraints) is defined based on the available (if any) information about the environment in measurement-campaign details and from the behaviour (shape of graphs) of the measurement results.
3. An optimal value for each parameter from second category of the input parameters is set by minimizing the error in fitting by searching within the defined constraints.

Since, the variance of spread in the distribution is more important than the shape of distribution curves [12]; therefore, the absolute difference of the true standard deviation (TSD) [12] and RMS-DS of the proposed analytical results with empirical data-sets is taken as goodness-of-fit metric for AoA and ToA results, respectively, to gauge the fitness in mapping. In Fig. 19(a), the main lobe in the measurement data is caused by the far-end scattering region. The angular span of the main-lob can help in determining an appropriate value for the axes of far-end scattering volume compared to the link distance, i.e., d/a_1. Its shape being similar to bell-shape indicate an equal value for major and intermediate axes and a significantly higher value for minor axes of far-end scattering volume, i.e., $a_1 = b_1$ and $c_1 \gg a_1$. Furthermore, no (very minor) peaks in the tails of the curve indicate an equal and very small value for all the axes of observing-end scattering volume, i.e., $a_1 = b_1 = c_1 \approx 0$. In Fig. 19(b) and (e), minor lobs along the tails of distribution indicate a higher value for the ratio between major and intermediate axes of observing-end scattering volume, i.e., more elliptical-shaped base by setting a high value for a_1/b_1. Decrease in angular span and increase in sharpness of the peaks in tails can be ensured by setting a higher value for minor axis compared to major axis of observing-end scattering volume, i.e., increasing a_1/c_1. In Fig. 19(c), a minor tilt in the main-lob can be adapted by setting the orientation of far-end scattering volume, i.e., $-\varrho \leq \theta_1 \leq +\varrho$, where ϱ is a small value proportional to the level of tilt. In Fig. 19(d), a wide angular span with two similar slanted peaks can be modeled by increasing the values for far-end major and intermediate axes compared to the link distance, such that the major-lob caused by far-end volume overlaps a large portion of minor-lobs caused by observing-end scattering volume. Minor slant in the peaks can be tweaked by adjusting the orientation of both far- and observing-end scattering volumes, i.e., adjusting θ_m. In Fig. 19(c), the more prominent peaks in the tails compared to the peak along LoS direction indicate a higher volume of observing-end compared to the far-end scattering region, i.e., $V_2 > V_1$. Establishing a direct relationship between the input geometric parameter of the model with physical parameters from the propagation environment is of high significance. The optimal setting of input physical and geometric parameters, for which a good agreement (based on TSD and RMS-DS) between measurement and analytical results is presented in Table II, for all the comparative graphs presented in the Fig. 18, 19, and 20. It can be witnessed that the proposed model can effectively model a dynamic range of outdoor and indoor radio propagation environments; which is due to high degree of flexibility in geometric parameters of the proposed model. The proposed model not only effectively models the peaks of distribution of energy in angular (specially) and temporal domains, but also the tails of distribution; which is unlike its counterparts in the literature. The absolute difference between TSD of analytical (Proposed) and empirical curves is observed to be 0.05°, 2.707°, 0.55°, 4.93°, 4.38°, and 1.42° in Fig. 19 (a), (b), (c), (d), (e), and (f), respectively. Moreover, the proposed model provides an improvement of 0.01°, 0.15°, 0.03°, 3.563°, 1.721°, and 4.722° in the accuracy of model fitness over measurement results shown in Fig. 19 (a), (b), (c), (d), (e), and (f), respectively, when compared to a notable 3D analytical model in the literature [17,

Trans. Emerging Tel. Tech. 2016; **00**:1–20
DOI: 10.1002/ett
Prepared using ettauth.cls

18]. Moreover, for indoor propagation environments, the difference in fitness of analytical (proposed) results over measurement data-sets is observed to be 0.12°, 3.55°, and 0.34° in Fig. 20 (a), (b), and (c), respectively. This good fit of the proposed analytical results on empirical data-sets establishes the validity and usability of the proposed model.

Acknowledging the importance of comparing the proposed analytical results with appropriate M2M environments' measurement results, authors have conducted an exhaustive search for availability of such empirical data-sets in the open literature. Among the available measurement data-sets presented in the open literature, most are ineligible, presented in graphical three-dimensional plots or contour maps, from which no numerical data can be reliably extracted. Overall, for all the propagation environments, only a few readable data-sets can be located, among which mostly are for outdoor environments. This limitation has restricted the authors to provide a comparison with only three indoor measurement results. However, to prove the validity and worth of the proposed model, a detailed comparison with the available outdoor and indoor measurement data-sets is presented. Furthermore, for M2M communication scenarios, a comparison of the proposed model with a notable analytical model in the literature [17, 18] and performed computer simulations is presented, where a good fit can be observed. The proposed model provides high degree of accuracy in modeling a certain targeted propagation environment (for M2M) compared to its counterparts in the literature. This high degree of accuracy is achieved at the cost of model's complexity. There may be practical applications, where high degree of accuracy is highly desirable even at very high computational complexity cost. Demands for such high accuracy in channel modeling of emerging wireless communication networks are obvious due to expected increase in the amount of antennas at BSs (highly direction links), increase in carrier frequency (millimeter Waves), decrease in elevation of BSs and size of cells, and increase in density of nodes with direct device-to-device links, etc. The proposed theoretical results can stand as a good reference for conducting measurement campaigns for M2M communication scenarios. The proposed performance analysis on azimuthal and elevational angular spread of M2M communication scenarios is also helpful in enhancing the data rates of MIMO streams and/or designing sharp and precise antenna beamwidths using planar antenna arrays in correspondence with vertical and horizontal spacing among antenna elements.

4. CONCLUSIONS

A 3-D statistical channel model with high degrees of flexibility in geometric parameters has been proposed for emerging M2M communication environments. The proposed model has been demonstrated to effectively model a dynamic range of radio propagation environments. Independently rotatable and scalable ellipsoids have been considered around both the nodes of a communication link and another bounding ellipsoid has been considered associated with maximum propagation delay. The effective illuminated scattering region has been designed with the overlap region of this ellipsoid with the scattering ellipsoids around Tx and Rx. Analytical expressions for joint and marginal PDFs of ToA and AoA have been derived. The impact of various physical channel parameters such as link distance, antenna heights, size and position of scattering region, as well as shape and orientation of scattering region on delay and angular spread has thoroughly been investigated. In order to establish validity of the proposed model, the obtained analytical results have been compared with simulation results and with various experimental datasets given for different propagation scenarios in the literature. A good fit of proposed analytical results on empirical data-sets has been observed, which establishes the validity and flexibility of the proposed model.

A mathematical relationship between input geometric parameters (like, major, intermediate, and minor axes of scattering volumes and their horizontal orientation) can be established with constellation of the real environment in vicinity of Tx and Rx nodes, by conducting an intensive measurement campaign for M2M propagation environments. The fitness error optimization based parameters selection strategy (for some of geometric parameters) has been followed rather constellation of propagation environment. There remains the scope, to conduct a thorough study to determine such relationship of input geometric parameters with a constellation of the real environment in the future. Moreover, another possible

Table II: Comparison of the proposed analytical model with empirical data-sets found in the literature.

Environment	Channel Statistics	Figure	Measurement Data-set	Measurement campaign region	Antenna(s) Elevation	Proposed model input Parameters' setting	Absolute difference in RMS-DS	Absolute difference in angular TSD
Outdoor (Macro and Micro)	ToA	Fig. 18(a)	K. I. Pedersen *et al.* [20] (Figure 11)	Downtown, Aarhus, Denmark.	Above Rooftop level.	$a_1/b_1/c_1$ = 3/1.5/1, $a_2/b_2/c_2$ = 1/0.83/0.71, $h_1 - h_2$ = 25m, $z_1 - z_2$ = 5m, d/a_1 = 20/11, $\lvert\theta_1 - \theta_2\rvert = 0^O$, τ_{span} = 3.64 μsec	0.087 μsec	-
		Fig. 18(b)	K. I. Pedersen *et al.* [20] (Figure 9)	Downtown, Aarhus, Denmark.	Above Rooftop level.	$a_1/b_1/c_1$ =3/2/1, $a_2/b_2/c_2$ = 3.4/1.7/1, $h_1 - h_2$ = 25m, $z_1 - z_2$ = 4m, d/a_1 = 3/1, $\lvert\theta_1 - \theta_2\rvert = 0^O$, τ_{span} = 3.66 μsec	0.135 μsec	-
		Fig. 18(c)	M. D. Batariere *et al.* [21] (Figure 6)	Chicago, Illinois.	Rooftop level.	$a_1/b_1/c_1$ =3/2/1, $a_2/b_2/c_2$ = 3.2/1.5/1, 15m, $h_1 - h_2$ = 22m, $z_1 - z_2$ = 4m, d/a_1 = 3/1, $\lvert\theta_1 - \theta_2\rvert = 0^O$, τ_{span} = 1.5 μsec μsec	0.174 μsec	-
	Azimuth AoA	Fig. 19(a)	K. I. Pedersen *et al.* [20] (Figure 10)	Downtown, Aarhus, Denmark.	Above Rooftop level.	$a_1/b_1/c_1$ = 9/2/7, $a_2/b_2/c_2$ = 1/1/1, $h_1 - h_2$ = 0m, $z_1 - z_2$ = 0m , d/a_1 = 6/1, $\lvert\theta_1 - \theta_2\rvert = 0^O$, τ_{span} = 0.85 μsec	-	0.05°
		Fig. 19(b)	B. H. Fleury *et al.* [22] (Figure 16)	Downtown Area, Aalborg, Denmark	unspecified	$a_1/b_1/c_1$ = 1.5/5/1, $a_2/b_2/c_2$ = 1/1.3/1 , $h_1 - h_2$ = 5m, $z_1 - z_2$ = 4m, d/a_1 = 5/1m, $\lvert\theta_1 - \theta_2\rvert = -17^O$, τ_{span} = 0.65 μsec	-	2.707°
		Fig. 19(c)	P. A. Matthews *et al.* [23] (Figure 7)	Open site, Valley area, flats and few buildings, Leeds, UK	Above Rooftop level	$a_1/b_1/c_1$ = 1/1.2/1 $a_2/b_2/c_2$ = 1.5/3/1, $h_1 - h_2$ = 0m, $z_1 - z_2$ = 0m, d/a_1 = 1.5/1m, $\lvert\theta_1 - \theta_2\rvert = 45^O$, τ_{span} = 0.56 μsec	-	0.55°
		Fig. 19(d)	C. Kloch *et al.* [24] (Figure 6)	Small Campus, Aalborg University.	Low ($\approx$ 4m).	$a_1/b_1/c_1$ = 3/1/14, $a_2/b_2/c_2$ = 25/50/1, $h_1 - h_2$ = 6m, $z_1 - z_2$ = 5m, d/a_1 = 1/1, $\lvert\theta_1 - \theta_2\rvert = -5^O$, τ_{span} = 0.68 μsec	-	4.93°
		Fig. 19(e)	K. I. Pedersen *et al.* [25] (Figure 5)	Downtown, Aarhus, Denmark.	Rooftop level.	$a_1/b_1/c_1$ = 1/1/1.5, $a_2/b_2/c_2$ = 1/20/11, $h_1 - h_2$ = 15m, $z_1 - z_2$ = 5m, d/a_1 = 3/1, $\lvert\theta_1 - \theta_2\rvert = 0^O$, τ_{span} = 1.1 μsec	-	4.38°
		Fig. 19(f)	K. I. Pedersen *et al.* [20] (Figure 14)	Riverside, Stockholm, Sweden.	Rooftop level (21m).	$a_1/b_1/c_1$ = 1/1.6/1.6, $a_2/b_2/c_2$ = 1/7/1, $h_1 - h_2$ = 19m, $z_1 - z_2$ = 6m, d/a_1 = 2.2/1, $\lvert\theta_1 - \theta_2\rvert = 159^O$, τ_{span} = 1.2 μsec	-	1.42°
Indoor (Pico and M2M)		Fig. 20(a)	X. Yin *et al.* [26] (Figure 8(b))	In-office (LoS Scenario)	1.5m	$a_1/b_1/c_1$ = 4.5/22/1, $a_2/b_2/c_2$ = 2.4/1.5/1, $h_1 - h_2$ = 0m, $z_1 - z_2$ = 0m , d/a_1 = 1/1, $\lvert\theta_1 - \theta_2\rvert = 8.5^O$, τ_{span} = 210 $n$sec	-	0.12°
		Fig. 20(b)	X. Yin *et al.* [26] (Figure 8(e))	In-office (NLoS Scenarios)		$a_1/b_1/c_1$ = 2/4/1, $a_2/b_2/c_2$ = 2.2/1.5/1, $h_1 - h_2$ = 0m, $z_1 - z_2$ = 0m , d/a_1 = 6/1, $\lvert\theta_1 - \theta_2\rvert = 42^O$, τ_{span} = 160 $n$sec	-	3.55°
		Fig. 20(c)	X. Yin *et al.* [26] (Figure 8(h))			$a_1/b_1/c_1$ = 1/2/0.8, $a_2/b_2/c_2$ = 1/1/1, $h_1 - h_2$ = 0m, $z_1 - z_2$ = 0m , d/a_1 = 1.5/1, $\lvert\theta_1 - \theta_2\rvert = 70^O$, τ_{span} = 0.85 μsec	-	0.34°

extension of the proposed model can be the consideration of multi-bounce scattering into the account.

ACKNOWLEDGEMENT

The authors would like to acknowledge the partial support by EU-funded ATOM-690750 research project, approved under the call H2020-MSCA-RISE-2015.

DOI: 10.1002/ett
Prepared using ettauth.cls

REFERENCES

1. Song Q, Nuaymi L, Lagrange X. Survey of radio resource management issues and proposals for energy-efficient cellular networks that will cover billions of machines. *EURASIP Journal on Wireless Commun. and Networking* 2016; **2016**(1):1–20.
2. Dhillon HS, Huang HC, Viswanathan H, Valenzuela RA. Power-efficient system design for cellular-based machine-to-machine communications. *IEEE Trans. Wireless Commun.* 2013; **12**(11):5740–5753.
3. Talha B, Pätzold M. Channel models for mobile-to-mobile cooperative communication systems: A state of the art review. *IEEE Veh. Technol. Mag.* 2011; **6**(2):33–43.
4. Le KN. On angle-of-arrival and time-of-arrival statistics of geometric scattering channels. *IEEE Trans. Veh. Technol.* 2009; **58**(8):4257–4264.
5. Khan NM, Simsim MT, Rapajic PB. A generalized model for the spatial characteristics of the cellular mobile channel. *IEEE Trans. Veh. Technol.* 2008; **57**(1):22–37.
6. Petrus P, Reed JH, Rappaport TS. Geometrical-based statistical macrocell channel model for mobile environments. *IEEE Trans. Commun.* 2002; **50**(3):495–502.
7. Zhou J, Jiang H, Kikuchi H. Generalized 3D scattering channel model with mimo antenna systems. *China Commun.* 2016; **13**(5):66–81.
8. Kong SH. TOA and AOD statistics for down link gaussian scatterer distribution model. *IEEE Trans. Wireless Commun.* 2009; **8**(5):2609–2617.
9. Olenko AY, Wong KT, Qasmi SA, Ahmadi-Shokouh J. Analytically derived uplink/downlink TOA and 2-D-DOA distributions with scatterers in a 3-d hemispheroid surrounding the mobile. *IEEE Trans. Antennas Propagation* 2006; **54**(9):2446–2454.
10. Janaswamy R. Angle of arrival statistics for a 3-d spheroid model. *IEEE Trans. veh. technol.* 2002; **51**(5):1242–1247.
11. Durgin GD, Rappaport TS. Theory of multipath shape factors for small-scale fading wireless channels. *IEEE Trans. Antennas Propag.* May 2000; **48**(5):682–693.
12. Nawaz SJ, Khan NM, Ramer R. 3-D spatial spread quantifiers for multipath fading wireless channels. *IEEE Wireless Commun. Lett.* Jul 2016; **5**(9):484–487.
13. Paul BS, Hasan A, Madheshiya H, Bhattacharjee R. Time and angle of arrival statistics of mobile-to-mobile communication channel employing circular scattering model. *IETE Journal of Research* 2009; **55**(6):275–281.
14. Baltzis KB. A simplified geometric channel model for mobile-to-mobile communications. *Radioengineering* 2011; **20**(4):961–967.
15. Baltzis KB. A generalized elliptical scattering model for the spatial characteristics of mobile channels. *Wireless Personal Commun.* 2012; **67**(4):971–984.
16. Zajic AG, Stuber GL. Three-dimensional modeling, simulation, and capacity analysis of space-time correlated mobile-to-mobile channels. *IEEE Trans. Veh. Technol.* 2008; **57**(4):2042–2054.
17. Riaz M, Nawaz SJ, Khan NM. 3D ellipsoidal model for mobile-to-mobile radio propagation environments. *Wireless Personal Commun.* 2013; **72**(4):2465–2479.
18. Nawaz SJ, Riaz M, Khan NM, Wyne S. Temporal analysis of a 3D ellipsoid channel model for the vehicle-to-vehicle communication environments. *Wireless Personal Commun.* 2015; **82**(3):1337–1350.
19. Baltzis KB. A geometric method for computing the nodal distance distribution in mobile networks. *Progress In Electromagnetics Research* 2011; **114**:159–175.
20. Pedersen KI, Mogensen PE, Fleury BH. A stochastic model of the temporal and azimuthal dispersion seen at the base station in outdoor propagation environments. *IEEE Trans. Veh. Technol.* Mar 2000; **49**(2):437–447.
21. Batariere MD, Blankenship TK, Kepler JF, Krauss TP, Lisica I, Mukthavaram S, Porter JW, Thomas TA, Vook FW. Wideband MIMO mobile impulse response measurements at 3.7 GHz. *Proc. of IEEE Veh. Technol. Conf.*, vol. 1, 2002; 26–30.
22. Fleury BH, Tschudin M, Heddergott R, Dahlhaus D, Pedersen KI. Channel parameter estimation in mobile radio environments using the sage algorithm. *IEEE J. Sel. Areas Commun.* 1999; **17**(3):434–450.
23. Matthews PA, Molkdar D, Mohebbi B. Direction of arrival and frequency response measurements at UHF. *Proc. of Int. Conf. on Mobile Radio and*

Personal Commun., IET, 1989; 43–47.

24. Kloch C, Liang G, Andersen JB, Pedersen GF, Bertoni HL. Comparison of measured and predicted time dispersion and direction of arrival for multipath in a small cell environment. *IEEE Trans. Antennas Propag.* 2001; **49**(9):1254–1263.
25. Pedersen KI, Mogensen PE, Fleury BH. Spatial channel characteristics in outdoor environments and their impact on BS antenna system performance. *Proc. of IEEE Veh. Technol. Conf.*, vol. 2, 1998; 719–723.
26. Yin X, Ling C, Kim MD. Experimental multipath-cluster characteristics of 28-GHz propagation channel. *IEEE Access* 2015; **3**:3138–3150.
27. Ziółkowski C, Kelner JM. Geometry-based statistical model for the temporal, spectral, and spatial characteristics of the land mobile channel. *Wireless Personal Commun.* 2015; **83**(1):631–652.
28. Ziółkowski C, Kelner JM. Estimation of the reception angle distribution based on the power delay spectrum or profile. *Int. Journal of Antennas Propag.* 2015; **15**.
29. Wong KT, Wu YI, Abdulla M. Landmobile radiowave multipaths' DOA-distribution: assessing geometric models by the open literature's empirical datasets. *IEEE Trans. Antennas Propag.* 2010; **58**(3):946–958.

DOI: 10.1002/ett
Prepared using ettauth.cls